Wall Pressure Fluctuations in an Axisymmetric Turbulent Boundary Layer under Strong Adverse Pressure Gradient

Conference Paper · January 2020

DOI: 10.2514/6.2020-0572

N. Agastya Balantrapu
University of Utah

Christopher Hickling
Virginia Tech (Virginia Polytechnic Institute and State University)

Aldo Gargiulo
Virginia Tech (Virginia Polytechnic Institute and State University)

Vidya Vishwanathan
Virginia Tech (Virginia Polytechnic Institute and State University)

Wall Pressure Fluctuations in an Axisymmetric Turbulent Boundary Layer under Strong Adverse Pressure Gradient

N. Agastya Balantrapu[1], Daniel J. Fritsch[1], Anthony J. Millican[1], Christopher Hickling[1], Aldo Gargiulo[1], Vidya Vishwanathan[1], W. Nathan Alexander[2], and William J. Devenport[3]

Virginia Tech Center for Research in Experimental Aero/hydrodynamic Technology (CREATe), Blacksburg, VA, 24061, USA

Measurements of wall pressure fluctuations in an axisymmetric turbulent boundary layer under a strong adverse pressure gradient are analyzed, in combination with Large Eddy Simulations [12,13]. Mean flow in the outer regions of this non-equilibrium boundary layer is self-similar with embedded shear layer scaling, and the associated large scale motions intensify under the adverse pressure gradient. The overall wall pressure levels drop as the flow decelerates downstream, and appear to scale best with the local wall shear stress τ_w – plateauing approximately at 7 τ_w. Consistent with the overall levels, auto-spectral densities collapse with τ_w as the pressure scale and Strouhal number based on local freestream velocity and boundary layer thickness $f\delta/U_e$. Overall, the intensified large motions in the outer region strongly influence both the near-wall turbulence and wall pressure, as seen in the streamwise space-time correlation structure of the unsteady velocity and wall pressure.

I. Introduction

TURBULENT boundary layers impose pressure fluctuations on underlying surfaces and are a strong source of structural vibrations and aeroacoustic noise, especially when the travelling turbulence encounters discontinuities, like the trailing-edge of airfoils. Furthermore, these wall pressure fluctuations are an integrated effect of the turbulent velocity field across the boundary layer [1] and understanding them could provide fundamental insight to the turbulence structure.

The fundamental case of planar, zero pressure gradient flows has been extensively investigated resulting in well-accepted models for both spectral density and the full wavenumber-frequency spectrum [2-5]. However, the effects of mean pressure gradients on the flow and therefore the wall pressure field are more complicated. Specifically, an adverse pressure gradient (APG) flow – like the rear of an airfoil, or the inlet and compressor stages of a turbine engine – decelerates the boundary layer, intensifies the large-scale motions dominating the outer regions and, if strong enough, could eventually lead to separation [6]. While recent investigations considered two-dimensional pressure gradient flows [7-11], we investigate the wall pressure field over a body of revolution, under a strong adverse pressure gradient. Analyzing the measurements of the flow structure and wall pressure field, in combination with Large Eddy Simulations [12,13], we will show that the mean flow of this non-equilibrium turbulent boundary layer is self-similar with the embedded shear scaling [14]. and the associated large-scale motions intensify in the outer regions, shifting further away from the wall; The overall wall pressure levels drop, and appear to scale with the wall-shear stress. The corresponding auto-spectral densities across the APG region collapse with wall-shear stress and Strouhal number

[1] Graduate Research Assistant, Crofton Dept. of Aerospace and Ocean Engineering, AIAA Student Member
[2] Assistant Professor, Crofton Dept. of Aerospace and Ocean Engineering, AIAA Member
[3] Professor, Crofton Dept. of Aerospace and Ocean Engineering, AIAA Associate Fellow

based on local edge velocity and boundary layer thickness. Overall, it appears as if the intensified large sale motions strongly influence the near wall turbulence and wall pressure field, as seen in both the turbulent velocity and wall pressure convection velocities. Preliminary comparisons with existing wall-pressure spectrum models for pressure gradient flows [7-11] outline the importance of the pressure gradient history and transverse curvatures.

In the following section we describe the experimental methods, including the apparatus, instrumentation and data reduction. Section III presents the analysis and discussion, followed by conclusions in Section IV.

II. Experimental Methods

A. Virginia Tech Stability Wind Tunnel

All measurements were performed in the anechoic test section of the Virginia Tech Stability Wind Tunnel (Figure 1), designed and documented by Devenport et al. [15]. The test-section is 1.83 m square, 7.3 m long and features tensioned Kevlar side walls that contain the flow while remaining acoustically transparent. Sound passing through the walls is absorbed into anechoic chambers, lined with acoustic foam wedges, designed to minimize reflections down to 190 Hz. The floor and ceiling are similarly treated with perforated metal panels, lined with Kevlar and backed by 0.457-m acoustic foam wedges. Additionally, the entire circuit is acoustically treated to minimize background acoustic reflections. Measurements were made at flow speed approximately 20 m/s corresponding to freestream turbulence intensity of 0.02%.

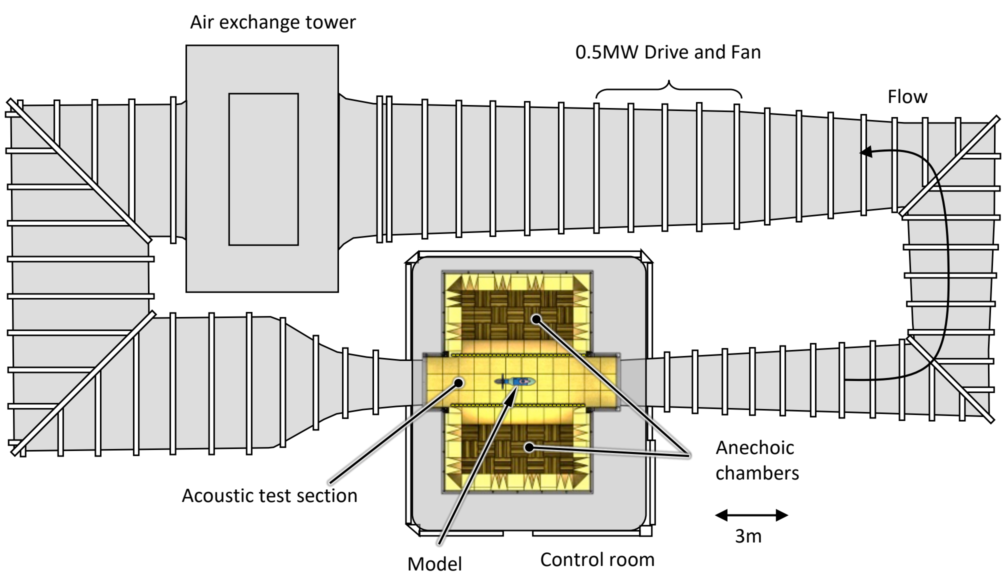

Fig. 1 Plan view of the closed circuit Virginia Tech Stability Wind Tunnel, with a removable test-section.

B. Body of Revolution and Co-ordinate system

The body-of-revolution (BOR) geometry, shown in Figure 2, is inspired from the work of Hammache et al [16], where they designed a body with a strong adverse pressure gradient on the aft ramp, generating a Stratford-Smith pressure distribution. With a characteristic length $D = 432\, mm$, our body of revolution consists of a forward $2{:}1$ ellipsoid nose and a cylindrical mid-body, with a 0.8 mm trip ring sandwiched at $x/D = 0.98$. At the rear, the mid-body transitions through a sharp corner onto a 20° tail cone. The tail cone angle was set through RANS simulations [17] and quarter-scale experiments ensuring attached flow throughout the adverse pressure gradient tail cone. This body of revolution is suspended at the nose by $0.9\, mm$ cruciform tethers and positioned downstream by a 0.76-m shaft fixed to a vertical post. The vertical post was faired by a 28% thick symmetric McMasters-Henderson airfoil to minimize the vortex shedding tones.

The co-ordinate system origin, shown in Figure 2, coincides with the nose, with the x-axis aligned with the centerline body. y is measured vertically upwards from the body centerline, and z-axis is positive towards the port side wall, completing a right-handed coordinate system. In the corresponding cylindrical co-ordinate system (r, ϕ, x) ϕ is measured from the y −axis, positive in anti-clockwise, when looking upstream.

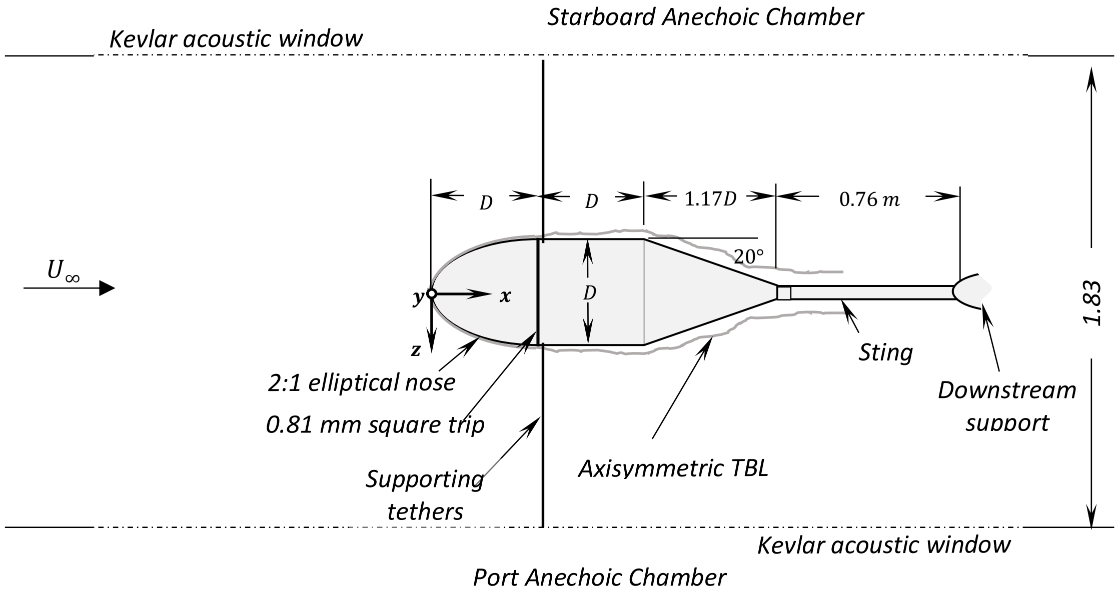

Fig. 2 Schematic of the BOR geometry and the experimental arrangement in the Stability Wind Tunnel test section. Co-ordinate system definition shown with the origin at the nose of the body.

C. Mean Surface Pressure Measurements

Mean pressure measurements were made using 85 half-millimeter surface pressure taps distributed across the body with 51 ports measuring the streamwise pressure distribution – shown in Figure 3 – while the remaining 34 taps, distributed over two concentric rings on the nose – at x/D = 0.095 and 0.50 – confirmed the circumferential uniformity. The mean pressure was sampled at 100Hz, with a 10" water range DTC Initium ESP-32HD acquisition system with 0.05% full-scale accuracy. Once the body was iteratively positioned at zero angle of attack to within 0.25° additional measurements with a custom-built total pressure rake, with 119 half-millimeter tubes was used to confirm axial symmetry in the flow at the BOR exit (x/D = 3.17) . Rake measurements were made with an Esterline 9816/98RK-1 NetScanner system with a 10" water range and a ± 0.03" water accuracy.

D. Unsteady Surface Pressure Measurements

The fluctuating wall pressure was measured on the BOR ramp with a streamwise linear array of 15 Sennheiser electret microphones (type KE-4-211-2), installed at $\phi = 292.5^\circ$ outside the influence of tether wakes, shown in Fig. 4. The microphones were nominally spaced by $12.7\ mm$ arranged between $x/D = 2.53$ to 3.08, and were fitted with $1\ mm$ pinhole caps, yielding a flat frequency response between $50 - 20{,}000\ Hz$. Primary measurements were made at the design Reynolds number based on the BOR diameter $Re_D = 600{,}000$, along with the measurements of the turbulence structure discussed in Section II. E. Further unsteady pressure measurements were made across Reynolds numbers ranging from $Re_D = 350{,}000$ to $750{,}000$ (in steps of 50,000). All measurements were made with a 24-bit Bruel & Kjaer LAN-XI data acquisition system, sampling at 65,536 Hz for 32 seconds, and anti-alias filtered at 25,600 Hz.

The one-sided spectral densities were estimated using the fast-Fourier transform algorithm in MATLAB by segmenting the time series into 511 blocks of 8192 samples, with a 50% overlap and using a Hanning window. Data at frequencies less than 50 Hz are discarded due to inadequate response of the microphones and background noise contamination. Similarly, data at frequencies with signal-to-noise ratio less than 10 dB are excluded. At $Re_D = 600{,}000$ the normalized pinhole diameter ($d^+ = du_\tau/\nu$) varied between 20 to 35 and is marginally above the limit of $d^+ = 18$ for under-resolving the high frequency fluctuations [18]; The high frequency limit corresponding to a 2-dB attenuation was estimated by extrapolating the criteria proposed by Gravante *et al.* [18] ($f\nu/U_\tau^2 \approx 0.22$ for $d^+ \approx$

26.6) and data above this frequency limit excluded. Furthermore, the contributions from vortex shedding past the 0.9 mm tethers were identified near 4500 Hz (corresponding to a Strouhal number ≈ 0.21) are discarded.

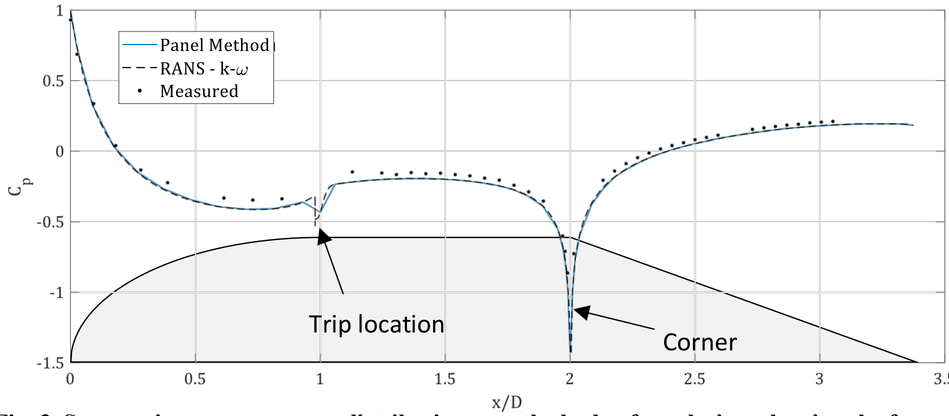

Fig. 3 Streamwise mean pressure distribution over the body of revolution, showing the favorable pressure gradient at the nose, a near-zero pressure gradient on the center body and an adverse pressure gradient region on the tail cone.

Fig. 4 Experimental photograph of streamwise array of flush-mounted Sennheiser microphones used to measure the unsteady surface pressure over the body of revolution tail cone

E. Measurements of Turbulent Velocity Field

Detailed measurements of the flow structure were made over the BOR ramp, using hotwire anemometry and Particle Image Velocimetry, described by Balantrapu *et al.* [19] and summarized here. A 1.2 mm single sensor hotwire probe manufactured by Auspex Corporation was used to document a 30-point profile of streamwise mean velocity, turbulence intensity and spectra of the boundary layer just upstream of the corner, at x/D = 1.97. Measurements over the ramp were made with a pair of single hotwire probes, over a 205-point grid from x/D = 2.05 to 3.17, across 15 streamwise stations. The single hotwire probes were spaced by 18.5 mm along a 9.3° line to the BOR axis; While the upstream probe measured the single-point streamwise velocity statistics and spectra, the combination of the probes provided estimates of the large-scale convection velocities of the streamwise unsteady velocity. Subsequently, the three-component velocity and six-component Reynolds stress tensor were measured over the same grid, using a miniature four-sensor AVOP-4-100 probe manufactured by Auspex corporation. The velocity and angle calibrations of the quad wire probe are discussed by Wittmer *et al.* [20]. The hotwires were calibrated frequently during measurements to account for temperature drift and corrections made according to Bearman's procedure [21]. Mean velocity and streamwise Reynolds normal stress estimates from the single hotwire are in agreement with those from planar Particle Image Velocimetry [19]. All hotwire measurements were made with a DANTEC 90N10 constant temperature anemometer, sampled by a National Instruments 9225-c9191 data acquisition module at 50,000 Hz, obtaining 50 independent records of 8192 samples each.

Since accurate measurements of wall-shear stress are particularly challenging and as the conventional techniques used for zero pressure gradient flows are not applicable for the adverse pressure gradient flows, for the purposes of this paper, we use the wall-shear stress from Wall-Resolved Large Eddy Simulations (WRLES) of the flow over the BOR [12,13], made at the same Reynolds number ($Re_D \approx 600{,}000$) and physical conditions consistent with the wind tunnel experiments. LES estimates of the mean pressure distribution on the BOR are in agreement with the experiments, and the unsteady wall pressure spectra on ramp are consistent to within 2 dB, particularly at the mid and high frequencies, where the viscous scales near the wall play a dominant role. This suggests that the skin friction estimates (Fig. 5) are reliable. In subsequent work we will confirm this with skin friction estimates based on recent work of Volino et al. [22] where they proposed a new analytical technique of estimating the skin friction, from the profiles of the streamwise velocity (based on the streamwise boundary layer momentum equation transformed in the inner co-ordinates).

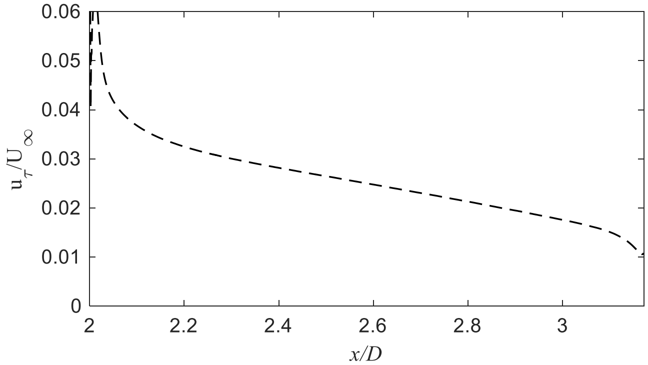

Fig. 5 Skin-friction velocity normalized on the tunnel reference velocity, obtained from Wal-Resolved LES.

III. Results and Discussion

Results will be discussed in the co-ordinate system presented in Section II. A; U, V, W represent mean velocities along the x, y, z axes respectively, while U_s represents the streamwise mean velocity. Similarly, the turbulent velocities are represented by lower case letters; u, v, w, u_s while the skin friction velocity is u_τ. U_∞ represents the tunnel freestream velocity while U_e is the local freestream velocity outside the boundary layer. The boundary layer velocity, displacement and momentum thicknesses will be δ, δ^* and θ respectively. While δ has been estimated as the location from the wall corresponding to a turbulence intensity of 2%, δ^* and θ are estimated according to the planar definitions.

A. Mean Flow over the BOR

Before entering the ramp, the boundary layer just upstream of the corner (x/D = 1.97) is 7.9 mm thick with a peak measured turbulence intensity of $0.08U_\infty$. The corresponding displacement and momentum thicknesses are 0.10δ and 0.07δ, with a shape factor $H = 1.44$ [19]. After experiencing a sharp local acceleration due to the corner, the flow decelerates on the ramp, by over 40% in the mean velocity, and the boundary layer thickens by a factor of 10, to 79.2 mm at the ramp exit (x/D = 3.17). The corresponding shape factor ($H = \delta^*/\theta$) increases from 2.5 to 3.3 across the ramp with the wall shear stress decreasing by about 75% over the ramp, from $0.04U_\infty$ at x/D = 2.1, to $0.01U_\infty$ at the ramp exit (Fig. 5). The pressure gradient parameters according to Castillo *et al.* [23] and Clauser [24], presented in equations 4 – 6 (Section III.C), vary across the ramp from 0.3 – 0 and 4 – 15 respectively, suggesting the flow is not in equilibrium. The corresponding streamwise Reynolds normal stress, shown in Fig. 6, develop an outer peak that shifts away from the wall, occurring at 0.6δ at the ramp exit. Based on spectral analysis of the Reynolds stresses, several studies attributed this peak to the intensified large scale motions in the outer regions [12, 13, 21, 22].

Despite the flow being out of equilibrium we find that the mean velocity and the turbulence intensities across the ramp are self-similar, based on the recently proposed Embedded Shear Layer scaling for large-defect boundary layers [25]. Shatzman *et al.* [25] observed that boundary layers under strong APG are characterized by coherent spanwise vorticity in the outer regions, resulting from inviscid instabilities – similar to free shear layers [26] – corresponding to an inflection point in the mean velocity profile. Inspired from prior work on mixing layers they proposed a velocity defect scale $U_d = U_e - U_{IP}$ where U_{IP} is the mean velocity at the inflection point. The corresponding length scale is the vorticity thickness defined as $\delta_\omega = U_d/|dU_s/dz|_{IP}$. They observed the mean flow and the streamwise turbulence intensities along the planar APG ramp to attain self-similarity with the new co-ordinates of $U^* = (U_e - U_s)\ /U_d$ and $\eta = (z - z_{IP})/\delta_\omega$. Though we observed inflection points in the mean velocity profiles, we found an improved scaling when the parameters based on streamwise Reynolds stress peak location are used instead of those at the inflection point, shown in Fig. 7. Furthermore, we find that the mean velocity profile in the outer regions ($\eta > 1$) can be represented by complementary error function $erfc(\eta) = 1 - \mathrm{erf}\,(\eta)$, used for fully developed mixing layers [27]. Some disagreement closer to the wall could perhaps come from the no-slip condition at the surface.

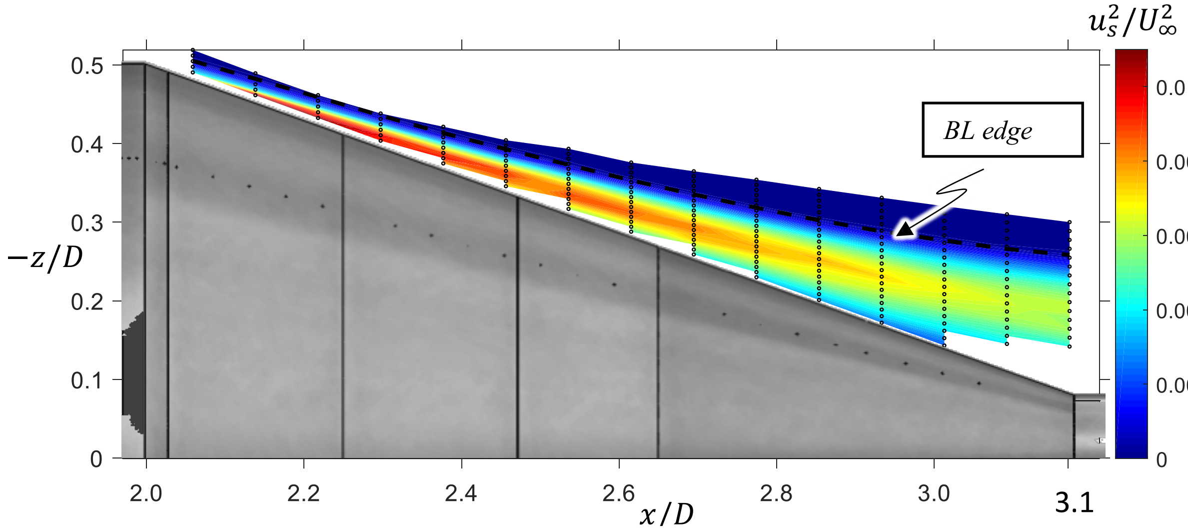

Fig. 6 Contours of streamwise Reynolds normal stress over the BOR ramp at $Re_D \approx 600{,}000$

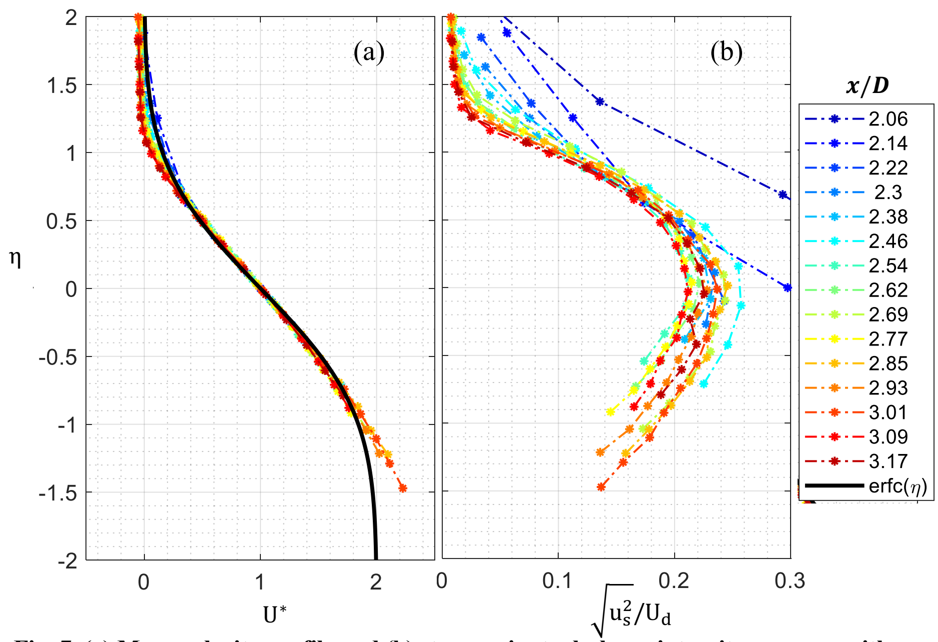

Fig. 7 (a) Mean velocity profile and (b) streamwise turbulence intensity on ramp with embedded shear layer scaling.

B. Wall Pressure Fluctuations on Ramp

The root-mean-square pressure fluctuations decrease as the flow decelerates over the BOR ramp and do not scale with the local freestream dynamic pressure, in contrast to the observations of Hu [11]. This could be due to the additional influence of the transverse curvature, as observed by Neves and Moin [28] in their study of flow past circular cylinders axially-aligned with the flow. Regardless, the RMS pressures scale with the local wall-shear stress, shown in Fig. 8, plateauing at approximately 7 τ_w, indicating the importance of near wall turbulence, despite the increase in the large-scale activity in the outer regions. When scaled on the peak streamwise Reynolds shear-stress $\rho u_s w_s$ from the quad-wire measurements, the levels are generally lower than the skin-friction based plateau, and show some downstream dependence. While the Reynolds stress uncertainty could be significant due to inherent quad-wire limitations [29], the decreasing trend could be due to the outer peak moving further away from the wall downstream (Fig. 6).

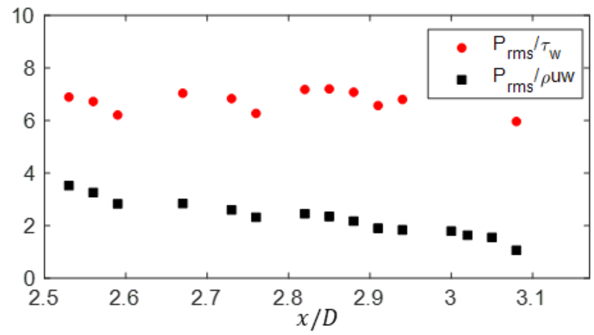

Fig. 8 Root mean-square levels of the unsteady wall pressure along the tail cone, normalized on wall shear stress and peak Reynolds shear stress

The one-sided raw auto-spectral densities of the wall pressure along the ramp, shown in Fig. 9(a), appear to shift towards lower frequencies, consistent with previous APG studies [7-11]. Further, we find the spectral densities across the adverse pressure gradient region collapse with a Strouhal number based on the boundary layer thickness and edge velocity: $f\delta/U_e$, and τ_w as the pressure scale, shown in Fig. 9(b). At lower frequencies, the spectral levels increase approximately as $f^{1.5}$ and peak at $f\delta/U_e \approx 0.15$. The overlap regions decay generally with a slope of about -1.5 , nearly twice the slope seen in zero pressure gradient case, and show some downstream dependence. The high frequency viscous roll-off is steeper at -5 and is consistent with planar, zero pressure-gradient studies, perhaps unaffected by the adverse pressure gradient.

Further investigations with different pressure scales and Strouhal numbers revealed that: 1) Consistent with over all levels, τ_w is the superior choice for pressure scale, compared to those based on peak Reynolds shear-stress, edge velocity or the shear layer defect velocity U_d; 2) With edge velocity, Strouhal number based on displacement thickness $f\delta^*/U_e$ produces a similar collapse as in Fig. 9(b), while that based on the shear layer vorticity thickness $f\delta_\omega/U_e$ is not as successful, especially at higher frequencies; 3) Strouhal number based on viscous-scales $f\nu/u_\tau^2$ collapses the high-frequency range comparable to Fig. 9(b). 4) In general, U_e based Strouhal numbers collapse the spectra better compared to u_τ and is justified as the broadband pressure convection velocities scale with U_e, shown in Fig. 10.

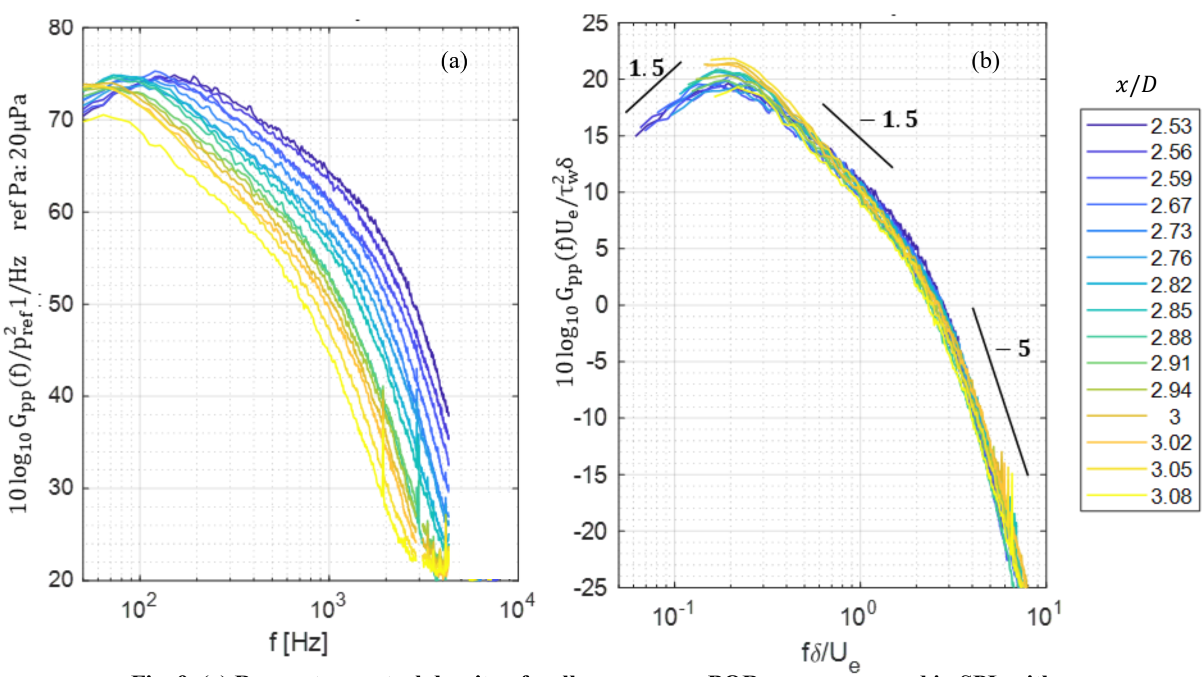

Fig. 9 (a) Raw auto-spectral density of wall pressure on BOR ramp expressed in SPL with $p_{ref} = 20\ \mu Pa$. (b) Normalized spectra, with wall shear stress (τ_w) as the pressure scale, and U_e/δ as the frequency scale.

The broadband phase convection velocities normalized on the local edge velocity are shown in Fig. 10, for each anchor microphone, as a function of the separation normalized on the boundary layer thickness. The convection velocities increase with separation, approaching a $0.6U_e$ asymptote across all anchor positions; This asymptote is considerably lower than the zero pressure gradient case ($0.8 - 0.85\ U_e$) due to reduced mean flow speeds under the

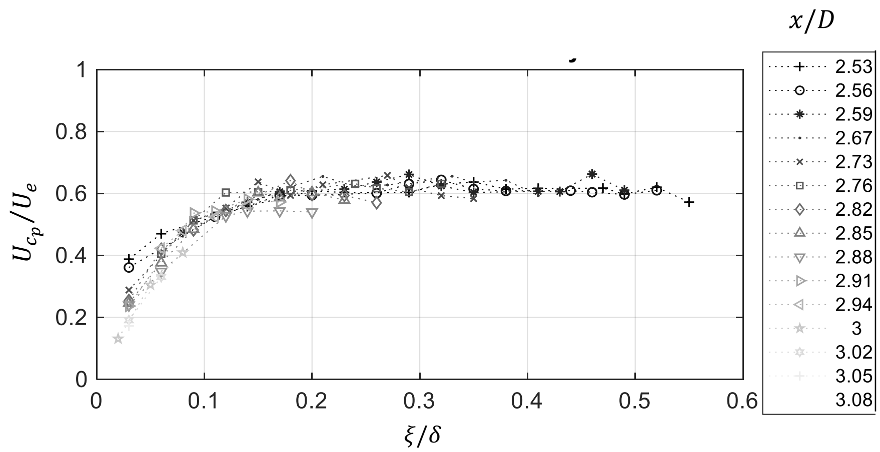

Fig. 10 Pressure convection velocity (U_{c_p}) normalized on the edge velocity (U_e) at the anchor mic, as a function of separation ($\xi = x - x'$) normalized on the δ at anchor microphone, shown for all anchor positions.

APG. The convection velocities of the streamwise turbulent velocity across the ramp are shown in Fig. 11; Turbulent structures in the outer regions convect at the local mean flow speeds across the ramp, while those near the wall ($< 0.2\delta$) travel significantly faster than the corresponding local mean, suggesting the influence of the faster moving structures on the near wall turbulence [19]. Furthermore, the pressure convection velocity from adjacent pairs of microphones across the ramp compare well with the near-wall convection velocities of the streamwise turbulent velocity, shown in the inset of Fig. 11. This, combined with the success of τ_w as the pressure scale, appears to indicate that, while the while near-wall turbulence continues to play an important role in the wall pressure fluctuation field,

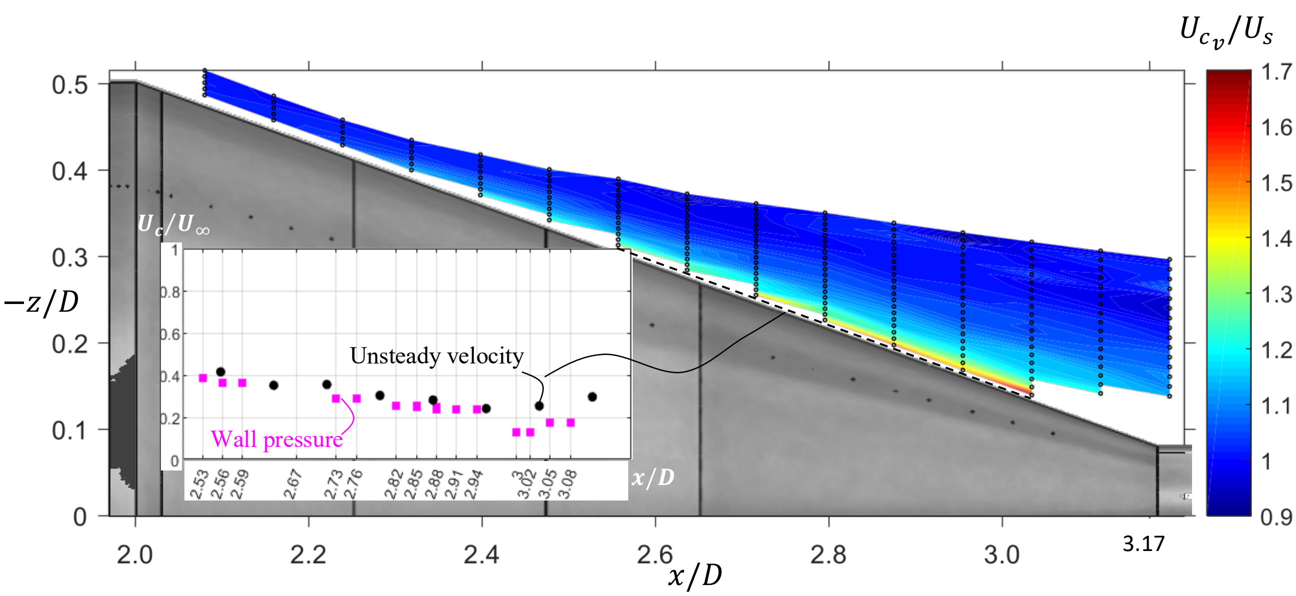

Fig. 11 Contours of convection velocity of the unsteady streamwise velocity (normalized on tunnel reference velocity U_∞), from dual single-hotwire measurements at $Re_D \approx 600{,}000$. Inset comparing the convection velocity from consecutive microphones ($12.7\ mm$ spacing), compared with those of the unsteady velocity from hotwire measurements near the wall (about $10 - 15\%$ boundary layer thicknesses above the wall).

the large-scale motions in the outer regions – intensified by the adverse pressure gradient – influence both near-wall turbulence and the hence the wall pressure fluctuations.

C. Comparisons with Wall Pressure Spectral Models

Several empirical wall pressure spectral models for pressure gradient flows were developed recently[7-11], based on experiments from flow past trailing edge of airfoils, planar wedges, and compressor blades. In general, all models have a structure similar to that originally proposed by Goody [2] for zero pressure gradient flows, shown in equation 1. Parameter a affects the overall amplitude, b determines slope at low frequencies while d determines the location of the peak; c, e control the slope at mid-frequencies, and h controls the slope at high frequency. Parameters f and g determine the extent of the overlap region, along with the ratio of the outer to viscous timescales $R_T = (\delta/U_e)/(\nu/u_\tau^2)$ which represents the Reynolds number effects.

$$G_{pp}(\omega)SS = \frac{a(\omega FS)^b}{[i(\omega FS)^c + d]^e + \left[(fR_T^g)(\omega FS)\right]^h} \tag{1}$$

With Goody's original model as the baseline case, we consider five models: 1) Rozenberg *et al*. [7] model for adverse pressure gradient flows; 2) Catlett *et al*. [8] model based on experiments in strong adverse pressure gradient past planar wedges; 3) Kamruzzaman *et al*. [9] model, based on experiments past airfoil and flat plate flows at different angles of attack, designed for both favorable and adverse pressure gradient flows; 4) Hu [11] model based on flat-plate flows placed under a rotating airfoil, designed for both adverse and favorable pressure gradients; 5) Lee [10] model, based on Rozenberg model, improved modified to work for a larger dataset. Parameters $a - h$ for each model are summarized in table 1-2, and are based on universal parameters (Δ, Π, β_c), defined in equations 2 – 4, represent the strength of the pressure gradient and the history effects, although the empirical constants differ in each case. The corresponding frequency and the spectral scale FS and SS for each model are listed in table 3; U_e is the common choice for the velocity scale except u_τ by Hu, while pressure scales differ between wall shear stress (Catlett, Kamruzzaman, Lee), peak Reynolds shear stress (Rozenberg) and the freestream dynamic pressure (Hu). The length scale is mostly displacement thickness δ^*, except δ by Catlett and momentum thickness θ, by Hu. A detailed comparison of the parameter choice for each model is provided by Lee [10].

Table 2. Parameters $a - d$ for the empirical wall pressure spectrum models

Model	a	b	c	d
Goody	3.0	2.0	0.75	0.5
Rozenburg	$[2.82\Delta^2(6.13\Delta^{-0.75}+d)^e][4.2\left(\frac{\Pi}{\Delta}\right)+1]$	2.0	0.75	$4.76\left(\frac{1.4}{\Delta}\right)^{0.75}[0.375e-1]$
Catlett	$3.0+e^{7.98}\left(\beta_\Delta Re_\Delta^{0.35}\right)^{0.131}-10.7$	2.0	$0.912 + 20.9\left(\beta_\delta Re_\delta^{0.05}\right)^{2.76}$	$0.397+0.328\left(\beta_\Delta Re_\Delta^{0.35}\right)^{0.310}$
Kamruzzaman	$0.45[1.75(\Pi_c^2\beta_c^2)^m+15, m=0.5\left(\frac{H_{12}}{1.31}\right)^{0.3}$	2.0	1.637	0.27
Lee	$\max(a,(0.25\beta_c-0.52)a)$, $a=[2.82\Delta^2(6.13\Delta^{-0.75}+d)^e][4.2(\Pi/\Delta)+1]$	2.0	0.75	$\max(1.0, 1.5d)$, $d=4.76(1.4/\Delta)^{0.75}[0.375e-1]$
Hu	$(81.004d+2.154)10^{-7}$	1.0	$1.5h^{1.6}$	$10^{-5.8\times10^{-5}Re_\theta H-0.35}$

Table 1. Parameters $e - h$ for the empirical wall pressure spectrum models

Model	e	f	g	h
Goody	3.7	1.1	-0.57	7.0
Rozenburg	$3.7+1.5\beta_c$	8.8	-0.57	$\min(3, 19/\sqrt{R_T})+7$
Catlett	$3.872 - 19.3\left(\beta_\delta Re_\delta^{0.05}\right)^{0.628}$	$2.19 - 2.57\left(\beta_\delta Re_\delta^{0.05}\right)^{0.224}$	$-0.5424 + 38.1(\beta_\delta H^{-0.5})^{2.11}$	$7.31 + 0.797\left(\beta_\delta Re_\delta^{0.35}\right)^{0.0724}$
Kamruzzaman	2.47	$1.15^{-2/7}$	$-2/7$	7.0
Lee	$3.7+1.5\beta_c$	8.8	-0.57	$\min\left(3, (0.139 + 3.1043\beta_c)\right)+7$
Hu	$1.13/h^{0.6}$	7.645	-0.411	6.0

Table 3. Parameters i, SS, and FS for the empirical wall

Model	i	SS	FS
Goody	1.0	$U_e/\tau_w^2\delta$	δ/U_e
Rozenburg	4.76	$U_e/\tau_{max}^2\delta^*$	δ^*/U_e
Catlett	1.0	$U_e/\tau_w^2\delta$	δ/U_e
Kamruzzaman	1.0	$U_e/\tau_w^2\delta^*$	δ^*/U_e
Lee	4.76	$U_e/\tau_w^2\delta^*$	δ^*/U_e
Hu	1.0	$u_\tau/Q^2\theta$	θ/U_e

$$\Delta = \delta/\delta^* \tag{2}$$

$$\Pi = \Pi_c = 0.8(\beta_c + 0.5)^{3/4} \tag{3}$$

$$\beta_c = \frac{\theta}{\tau_w}\frac{\partial p}{\partial x};\ \beta_{\delta^*} = \frac{\delta^*}{\tau_w}\frac{\partial p}{\partial x} \tag{4}$$

$$\Lambda = -\frac{\delta}{U_e(d\delta/dx)}\frac{dU_e}{dx} \tag{5}$$

Comparison of each of the models against the experimental results and Goody model for reference are shown in Fig. 12, for three representative locations on the ramp. The results are mixed: no model appears to consistently agree with the measurements across the ramp. Initially, both Rozenberg and Lee models predict the measurements well, particularly at the mid and high frequencies, capturing both the amplitude and decay rates accurately. Note that we have used wall-shear stress as the pressure scale in Rozenberg's model against the original shear stress peak, in the wake of our observations in Section III. B. Agreement with Kamruzzman model improves downstream and appears to accurately predict both the overall levels and shape, at least for $x/D = 3.05$. Catlett *et al.'s* model generally underpredicts the low and mid frequencies by about 15 dB/hz, consistent with Lee's observations [10]. Hu's model initially underestimates the low frequency levels while overpredicting them downstream. From the contours of SPL difference in Fig. 13, shown with frequency versus the streamwise position, for each model, it appears as if all current models underpredict the low frequency levels, agree with our measurements best in the overlap regions, while over-predicting the high frequency levels. To some extent this highlights the sensitivity of the wall pressure fluctuations to the pressure gradient history, and the transverse curvature effects, particularly towards the BOR exit, where the local

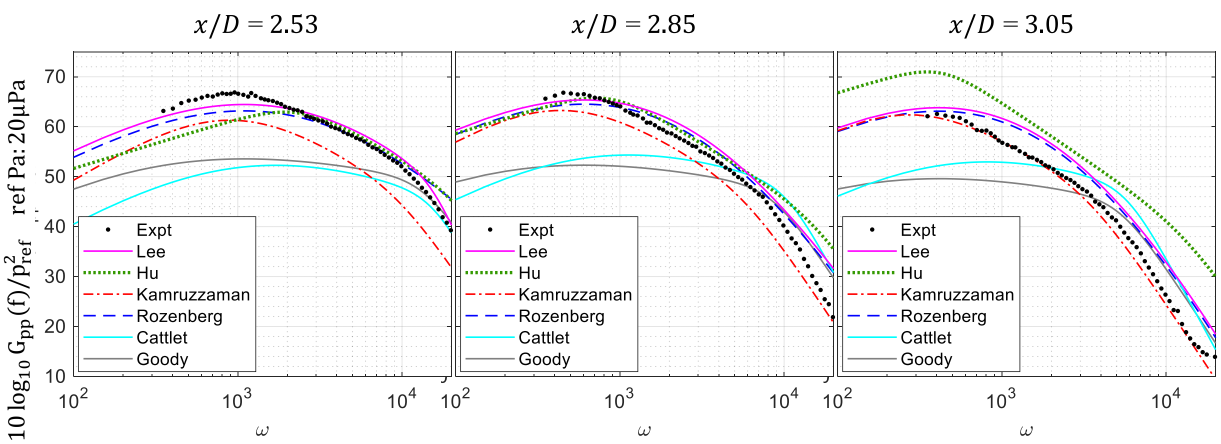

Fig. 12 Comparison of wall pressure spectra with empirical models from literature.

radius based Reynolds number ($r^+ = ru_\tau/\nu$) decrease to about 1000 - where the transverse curvature begins to affect the near wall flow [28].

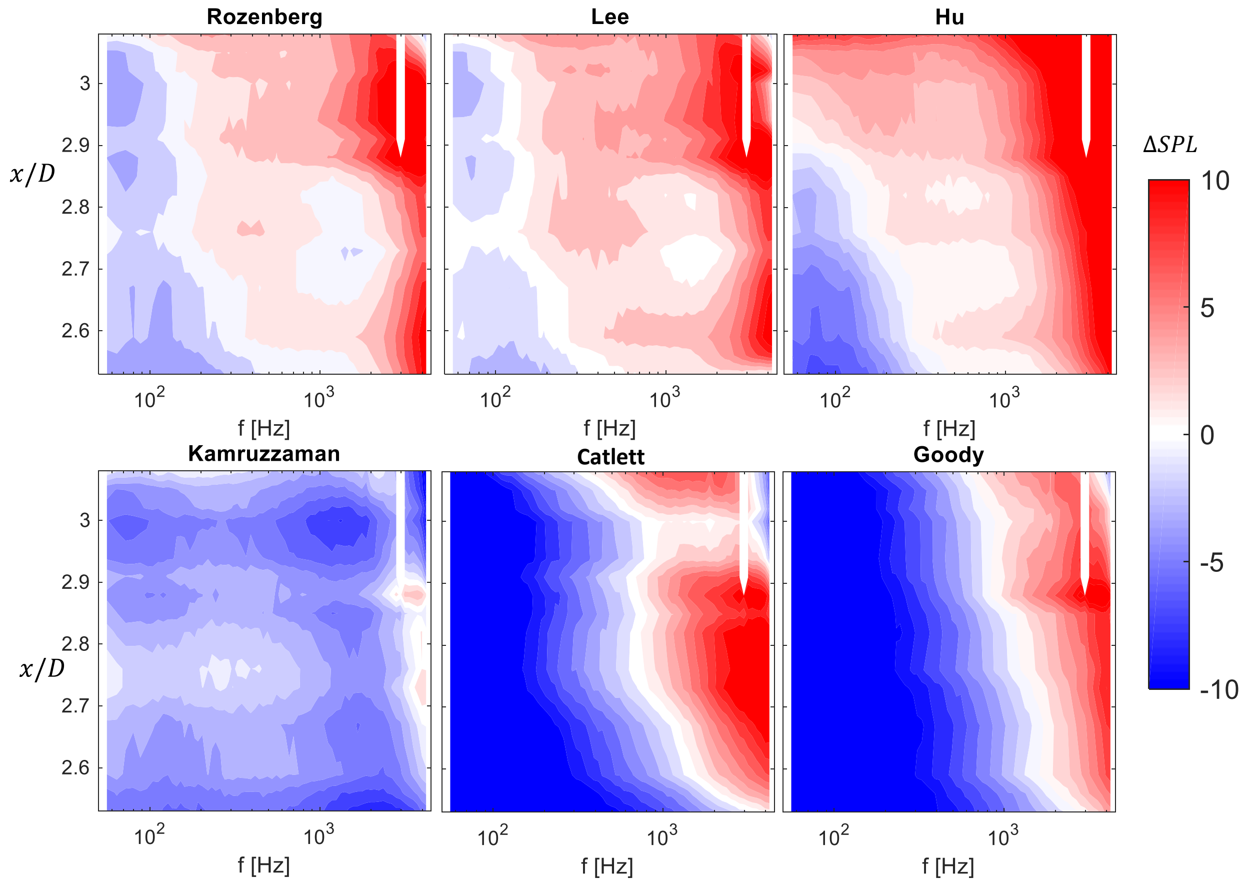

Fig. 13 Contours of the SPL difference between the measurements and empirical models, as a function of frequency and position on the BOR ramp.

IV. Conclusions

Measurements of the turbulence structure and the wall pressure fluctuations of an axisymmetric turbulent boundary layer under a strong adverse pressure gradient are analyzed, in combination with LES [13]. The mean flow of this non-equilibrium boundary layer is self-similar in the outer regions with embedded shear layer scaling [25]. The associated large scale motions are intensified under adverse pressure gradient, while the skin friction decrease continuously. The wall pressure fluctuation statistics appear to be dominated by near-wall motions, with the root-mean square levels roughly 7 τ_w across the APG region. The corresponding auto-spectral densities scale with wall shear stress as the pressure scale and the outer boundary layer scales δ/U_e as the time scale, suggesting the importance of the motions across the boundary layer, even under the adverse pressure gradient. Particularly, the intensified large scale motions in the outer regions appear to dominate the near wall turbulence as seen in both the pressure and the velocity convection velocities.

Comparison of wall pressure spectra with existing empirical models for 2-dimensional, pressure gradient flows [7-11] provided mixed results. While all models generally underpredict the low frequency amplitude, Rozenberg's model with wall-shear stress as the pressure scale predict the overlap regions within 3 dB. However, all models overpredict the high frequency regions by about 5 - 10 dB outlining the importance of pressure gradient history and transverse curvature on the wall pressure fluctuations.

Acknowledgements

We thank the Office of Naval Research, particularly, Drs. Ki-Han Kim and John Muench and Peter Chang, for support through grants N00014-18-1-2455, N00014-17-1-2698, N00014-18-1-2304, N00014-19-1-2109. We are grateful to Dr. Meng Wang and Di Zhou for providing us with data from LES. We are grateful to Dr. Stewart Glegg for helpful advice and support. We also acknowledge the support from the Virginia Tech Aerospace and Ocean Engineering machine shop, headed by Mr. James Lambert. Many thanks to Bill Oetjens, Nandita Hari, James MacDonald, and other graduate researchers for assisting with the wind tunnel experiments.

References

[1] Bull, M. K. (1996). "Wall Pressure Fluctuations Beneath Turbulent Boundary Layers: Some Reflections on Forty Years of Research." *Journal of Sound and Vibration* 190(3): 299-315.

[2] Goody M., “Empirical Spectral Model of Surface Pressure Fluctuations,” *AIAA Journal,* 2004, 49, no. 9

[3] Chase, D.M., *Modeling the Wavevector-Frequency Spectrum of Turbulent Boundary Layer Wall Pressure.* Journal of Sound and Vibration, 1980. **70**(1): p. 29-67.

[4] Corcos, G.M., *The structure of the turbulent pressure field in boundary-layer flows.* Journal of Fluid Mechanics, 1964. **18**(3): p. 353-378.

[5] Graham, W.R., *A Comparison of Models for the Wavenumber-Frequency Spectrum of Turbulent Boundary Layer Pressures.* Journal of Sound and Vibration, 1997. **206**(4): p. 541-565.

[6] Nagano, Y., et al. (1993). “Effects of adverse pressure gradients on mean flows and turbulence statistics in a boundary layer,” Proceedings of the 8th International Symposium on Turbulent Shear Flows, Sep 9 - 11 1991, Munich, Germany, Springer-Verlag New York.

[7] Rozenberg, Y., Robert, G., and Moreau, S., "Wall-Pressure Spectral Model Including the Adverse Pressure Gradient Effects." *AIAA journal* 2012, **50**(10): pp. 2168-2179.

[8] Catlett, M. R., Forest, J. B., Anderson, J. M., and Stewart, D.O., "Empirical modeling of pressure spectra in adverse pressure gradient turbulent boundary layers." *AIAA Journal,* 2014, **54**(2): pp. 569-587

[9] Kamruzzaman, M., Bekiropoulos, D., Lutz, T., and Würz, W., “A semi-empirical surface pressure spectrum model for airfoil trailing-edge noise prediction.” *International Journal of Aeroacoustics,* Vol. 14, 2015

[10] Lee, S., “Empirical Wall-Pressure Spectral Modeling for Zero and Adverse Pressure Gradient Flows,” *AIAA Journal,* Vol. 56(5), 2018, p. 1818-1829

[11] Hu, N., “Empirical spectral model of wall pressure fluctuations including adverse pressure gradient effects.” *AIAA Aviation Forum,* June 5-9 2017, 2017-3203

[12] Zhou, D., K. Wang, and M. Wang, *Large-Eddy Simulation of Axisymmetric Boundary Layer on a Body of Revolution*, in *AIAA Aviation 2020 Forum* (under preparation).

[13] Zhou, D., K. Wang, and M. Wang. *Large-eddy simulation of turbulent flow over a body of revolution*. in *J Bulletin of the American Physical Society*. 2019.

[14] Harun, Z., et al., *Pressure gradient effects on the large-scale structure of turbulent boundary layers.* Journal of Fluid Mechanics, 2013. **715**: p. 477-98.

[15] Devenport, W., Burdisso, R., Borgoltz, A., Ravetta, P., Barone, M., Brown, K., Morton, M., “The Kevlar-walled anechoic wind tunnel,” *Journal of Sound and Vibration,* 2013, vol. 332, no. 17, p. 3971-3991

[16] Hammache, M., F. Browand and R. Blackwelder (2002). "Whole-field velocity measurements around an axisymmetric body with a Stratford–Smith pressure recovery." *Journal of Fluid Mechanics,* 2002, 461: 1-24.

[17] Wang, M. (2018). Personal Communication.

[18] Gravante, S.P., et al., *Characterization of the Pressure Fluctuations Under a Fully Developed Turbulent Boundary Layer.* AIAA Journal, 1998. **36**(10): p. 1808-1816.

[19] Balantrapu, N. A., Hickling C.J., Millican A.J., Vishwanathan, V., Garguilo, A., Alexander W.N., Lowe K.T., Devenport, W.J., and Glegg, S.A.L., “Turbulent Boundary Layer in a Strong Adverse Pressure Gradient over a Body of Revolution.”11th International Symposium on Turbulence and Shear Flow Phenomena, 2019

[20] Wittmer, K.S., W.J. Devenport, and J.S. Zsoldos, *A four-sensor hot-wire probe system for three-component velocity measurement.* Experiments in Fluids, 1998. **24**(5): p. 416-423.

[21] Bearman, P.W., *Corrections for the effect of ambient temperature drift on hot-wire measurements in incompressible flow.* DISA Information, 1971. **11**: p. 25-30.

[22] Volino, R.J. and M.P. Schultz, *Determination of wall shear stress from mean velocity and Reynolds shear stress profiles.* Physical Review Fluids, 2018. **3**(3): p. 034606.

[23] Castillo, L., and George, W., "Similarity analysis for turbulent boundary layers with pressure gradient: outer flow," *AIAA Journal,* Vol. 39(1), 2001, p. 41-47

[24] Clauser, F., "The Turbulent Boundary Layer," *Advanced Applied Mechanics,* 1956, 4: p. 1-54

[25] Schatzman, D.M. and F.O. Thomas, *An experimental investigation of an unsteady adverse pressure gradient turbulent boundary layer: embedded shear layer scaling.* Journal of Fluid Mechanics, 2017. **815**: p. 592-642.

[26] Wygnanski, I. and H.E. Fiedler, *The two-dimensional mixing region.* Journal of Fluid Mechanics, 1970. **41**(2): p. 327-361.

[27] Pope, S.B., *Turbulent flows*. 2001, IOP Publishing.

[28] Neves, J.C. and P. Moin, *Effects of convex transverse curvature on wall-bounded turbulence. Part 2. The pressure fluctuations.* Journal of Fluid Mechanics, 1994. **272**: p. 383-406.

[29] Tutu, N.K. and R. Chevray, *Cross-wire anemometry in high intensity turbulence.* Journal of Fluid Mechanics, 1975 71(4): p. 785-800.